RMS1000
RAMAN MICROSCOPE

Extending the capabilities to Photoluminescence Microscopy, Time-Resolved Measurements and Fluorescence Lifetime Imaging (FLIM)

> Truly Confocal
> Five-Position Grating Turrets
> Two Spectrograph Options
> Up to Four Simultaneous Detectors

www.edinst.com

Journal of RAMAN SPECTROSCOPY WILEY

Raman analysis of a shocked planetary surface analogue: Implications for habitability on Mars

Melissa McHugh[1] | John Parnell[2] | Ian B. Hutchinson[1] |
Hannah N. Lerman[1] (ORCID) | Howell G.M. Edwards[1] | Mark J. Burchell[3] |
Mike J. Cole[3] | Andoni Moral[4] | Guillermo Lopez-Reyes[5] | Carlos Perez[4] |
Aurelio Arranz[5] | Marco Veneranda[5] | José Antonio Manrique[5] | Fernando Rull[5]

[1]School of Physics and Astronomy, University of Leicester, Leicester, UK

[2]School of Geosciences, University of Aberdeen, Aberdeen, UK

[3]School of Physical Sciences, University of Kent, Canterbury, Kent, UK

[4]Instituto Nacional de Técnica Aeroespacial (INTA), Madrid, Spain

[5]Unidad Asociada UVa – CSIC al Centro de Astrobiologia, University of Valladolid, Valladolid, Spain

Correspondence
Melissa McHugh, School of Physics and Astronomy, University of Leicester, University Road, Leicester LE17RH, UK.
Email: mm875@leicester.ac.uk

Abstract

The scientific aims of the ExoMars Raman laser spectrometer (RLS) include identifying biological signatures and evidence of mineralogical processes associated with life. The RLS instrument was optimised to identify carbonaceous material, including reduced carbon. Previous studies suggest that reduced carbon on the Martian surface (perhaps originating from past meteoric bombardment) could provide a feedstock for microbial life. Therefore, its origin, form, and thermal history could greatly inform our understanding of Mars′ past habitability. Here, we report on the Raman analysis of a Nakhla meteorite analogue (containing carbonaceous material) that was subjected to shock through projectile impact to simulate the effect of meteorite impact. The characterisation was performed using the RLS Simulator, in an equivalent manner to that planned for ExoMars operations. The spectra obtained verify that the flight-representative system can detect reduced carbon in the basaltic sample, discerning between materials that have experienced different levels of thermal processing due to impact shock levels. Furthermore, carbon signatures acquired from the cratered material show an increase in molecular disorder (and we note that this effect will be more evident at higher levels of thermal maturity). This is likely to result from intense shearing forces, suggesting that shock forces within basaltic material may produce more reactive carbon. This result has implications for potential (past) Martian habitability because impacted, reduced carbon may become more biologically accessible. The data presented suggest the RLS instrument will be able to characterise the contribution of impact shock within the landing site region, enhancing our ability to assess habitability.

KEYWORDS

analytical instrumentation, astrobiology, carbon, ExoMars, Raman spectroscopy

1 | INTRODUCTION

In the last decade, Raman spectroscopy has been identified as a powerful technique for the in situ analysis of surface material during planetary exploration surface missions.[1–3] Recent developments in instrument miniaturisation, robustness, and autonomy have led to Raman spectrometers being included on two of the most recent surface missions to Mars: there are two Raman systems on board NASA's Perseverance rover payload (launched in 2020),[4,5] and a Raman spectrometer is included in the ESA ExoMars Rover's suite of analytical instruments.[6]

ExoMars is a joint European Space Agency and Roscosmos mission developed as part of ESA's Aurora programme.[7] The first part of the mission incorporated the Trace Gas Orbiter (which successfully arrived at Mars in 2016[8]), and the second part will include deployment of a rover in 2023. The primary scientific aims of the ExoMars rover mission[9] are to (i) investigate and characterise the geology in terms of the habitability of the Martian surface (and sub-surface) in the search for biological signatures and mineralogical evidence of processes associated with past and present life; (ii) to determine the mineralogy, chemistry, and the origin of the Martian surface; and (iii) to characterise the water and geochemical environment as a function of depth in the Martian subsurface. The rover is due to land in the large clay-bearing plain of Oxia Planum,[10] a region that exhibits evidence of a diverse aqueous history, according to orbital data.[11]

In order to optimise the mission's ability to achieve the goal of searching for signs of extant or extinct life, the rover will be equipped with an autonomous 2-m drill.[9] Samples collected from the shallow subsurface by the drill will be crushed (with a typical grain size in the range 200–250 μm) and passed via the Sample Preparation and Distribution System (SPDS)[9] to a suite of instruments in the Analytical Laboratory Drawer (ALD), including the Raman laser spectrometer (RLS).[6] The RLS instrument will play a key role in achieving the majority of the mission aims. The instrument was specifically designed to enable the detailed characterisation of the geochemistry and water environment, and in particular, to be able to identify mineral phases linked with water–rock interactions.[6]

The key characteristics of the RLS instrument[12] are:

- The excitation source is a DPSS continuous wavelength of 532-nm laser;
- The optical head will deliver an irradiance of 0.4–8 kW cm^{-2} (with a laser spot size of 50 μm) at the sample; and

- The spectrometer, along with a cooled CCD detector, will provide a spectral range of 150–3800 cm^{-1} at a resolution of 6–8 cm^{-1}.

The instrument incorporates an autofocus mechanism that is able to move the optics over a 1-mm range and uses a feedback algorithm to maximise the intensity of the laser reflection, thereby maximising the spectroscopy signal. The spatial resolution achievable by the optical head is of the order of ∼2 μm. Spectra will be acquired on time scales of 0.1–60 s using optimised CCD operating modes and spectral extraction techniques (based on the strength of the Raman signal and fluorescence signal observed).[13]

The ability of the RLS instrument to discern between materials with varying states of hydration, different forms of carbonaceous material, and the impact of historical stress-related geological processes will play an important part in enabling the scientific goals of the ExoMars surface mission to be met. As such, a number of recent laboratory studies have focused on the use of portable Raman spectrometers to demonstrate how such instruments can detect and characterise a variety of sulphate and carbonaceous materials in a variety of natural, mineral matrices in preparation for mission operations.[9] Hutchinson et al. specifically investigated the ability of miniaturised instruments such as the RLS to detect carbon in samples that had been exposed to high levels of oxidation and described how the acquired spectra could be used to infer the thermal maturity of the samples.[14]

Carbonaceous materials often degrade under extreme environmental conditions resulting in simple, ordered structures, typically referred to as reduced carbon (i.e., sp^2 hybridised solid crystalline carbonaceous material). Such material has been theorised to be a provider of feedstock for microbial life and could therefore indicate a potential habitat.[15] Reduced carbon structures are expected to be present on the surface of Mars due to the erosion of carbonaceous volcanic rock,[16] past meteor bombardment,[17] or as a product of ancient biological processes[18]; that is, its origin could be biotic or abiotic, or could be a result of ancient carbonaceous meteorites.[19] Although reduced carbon has not yet been observed directly on the Martian surface, it has been identified within Martian meteorites, for example, in veinlets of carbonaceous matter in the Nakhla meteorite.[20] The attribution of nakhlite meteorites to Mars[21] makes them, and terrestrial analogues for them, particularly useful to study in support of Martian exploration. Organic compounds have also been encountered preserved in shallow drill holes made by the Curiosity rover.[22]

Whilst Raman spectroscopy cannot be used to directly infer origin, it can be used to identify differences in the

structural arrangement of carbonaceous matter (e.g., Wang et al.[23]). Laboratory-based studies[24,25] have also shown that the widths, position, and intensity ratios of carbon G and D bands directly relate to the material crystallinity, or degree of graphitisation (thermal maturity, expressed as ordering) within the carbon structures. Several other studies have also highlighted how Raman spectra can reflect changes at an atomic and molecular level due to ageing and regional metamorphism.[26]

The Raman technique is ideally suited to the investigation of carbonaceous material: chemical bonds such as the sp^2 hybridised (graphite like) and sp^3 hybridised (diamond-like) bonds exhibit strong Raman cross sections,[24] resulting in unambiguous spectral signatures, from which structural information can be determined, even with the compromises made with miniaturised instrumentation. A large number of studies have already been performed on the analysis of reduced carbon in meteorites[15,27] and in a range of terrestrial samples.[28–31] Recent investigations focusing on Archean rock samples have shown that the carbonaceous material present in the samples can be differentiated (spectrally) into populations based on levels of thermal maturity; that is, the characteristics of the so-called carbon D and G bands (Raman shifts of around 1350 cm^{-1} and between 1580 and 1600 cm^{-1}, respectively[23]) can be used as indicators of structural organisation within the carbon. The G (graphite) band is produced by the relative motion of carbon atoms in sp^2 bonded carbon (i.e., with 6-fold symmetry) and is therefore predominant in spectra obtained from graphite. The D (diamond) band results from sp^3 bonds in aliphatic carbon chains (i.e., with tetrahedral symmetry) and is hence forbidden in perfectly graphitic material.[32] Carbonaceous material typically exhibits both G and D bands due to the presence of edge effects or disorder in the sp^2 bonded material.

Nakhlite meteorites are olivine-pyroxene cumulates with secondary materials notably Fe-rich carbonates, sulphates, ferric saponite, and serpentine.[33,34] The clay and carbonate content resulted from the interaction of CO_2-charged fluids with surrounding nakhlite parent rocks[35]—they are hence considered key in our understanding of Martian surface mineralogy, as well as historical geological and atmospheric processes.[36] Nakhlite meteorites and their analogues are also ideal for assessing the capabilities of the RLS instrument due to similarities between the constituent minerals and phases expected to be present at Oxia Planum.

Here, we report on the Raman analysis of a Nakhla meteorite analogue that was partially subjected to stress through a projectile impact. Planetary surfaces, including Mars, have been substantially modified by meteorite bombardment, which are evident as impact craters up to hundreds of kilometres diameter. Within and around the craters, rocks are altered by mechanical and thermal shock, which may have modified the Raman characteristics of the constituent minerals. The minerals show defects from their original crystal structure, which is evident in Raman spectra.[37] Carbonaceous matter also shows modification, by changes in thermal maturity, which are similarly evident in Raman spectra. The effects of meteorite impact can be investigated using high velocity projectile impacts enabled by a light gas gun.

The analogue sample was an ancient carbon-bearing basalt collected in the United Kingdom. The embedded carbonaceous material, analogous to carbon in nakhlites, was incorporated during the thermal alteration of underlying shales.[38]

Sample characterisation was performed in a manner equivalent to that planned for ExoMars mission operations using the RLS Simulator, located at the Centre de Astrobiologia.[39] We discuss how thermal history and shock impacts of a sample affect the Raman spectra observed and determine the level to which such signatures can be identified when using the flight representative instrument.

2 | METHODOLOGY

2.1 | Helen's Bay analogue sample geological setting and key characteristics

The Martian analogue sample used for this study originated from an ancient basalt pillow lava at Helen's Bay, County Down, Northern Ireland (Irish Grid Reference J459831) (Figure 1). The basalt is Upper Ordovician (Caradoc) age and has been subject to greenschist metamorphism. Details of the locality are given by Sharpe[40] and Craig.[41]

The sample (shown in Figure 2) is a 4 × 4 cm block cut from a large basalt outcrop. The basalt contains 0.15–0.20 wt.% organic carbon and is cut by veinlets of calcite up to 2-mm width.

The basaltic material within the sample provides an analogue to the Nakhla meteorite (a Martian meteorite thought to originate from basaltic magma[38]). The veinlets on the sample surface are analogous to those seen in the Nakhla meteorite, which were found to contain sulphates, halides, and phyllosilicates.[42] These minerals are also expected at the Martian surface.[10] Most importantly to the analogy, the Helen's Bay sample contains reduced carbon[43] incorporated during basalt formation.

FIGURE 1 Geographical location of Martian analogue site, Helen's Bay, Northern Ireland
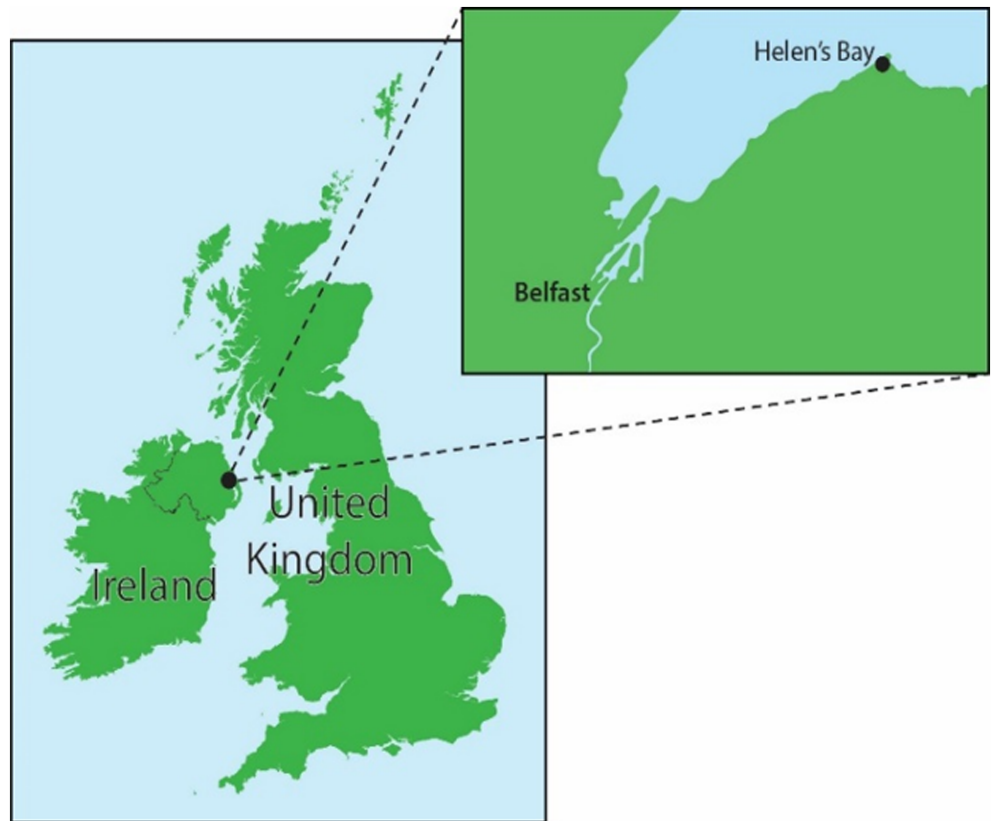
FIGURE 2 Nakhlite meteorite analogue sample from Helen's Bay, Northern Ireland
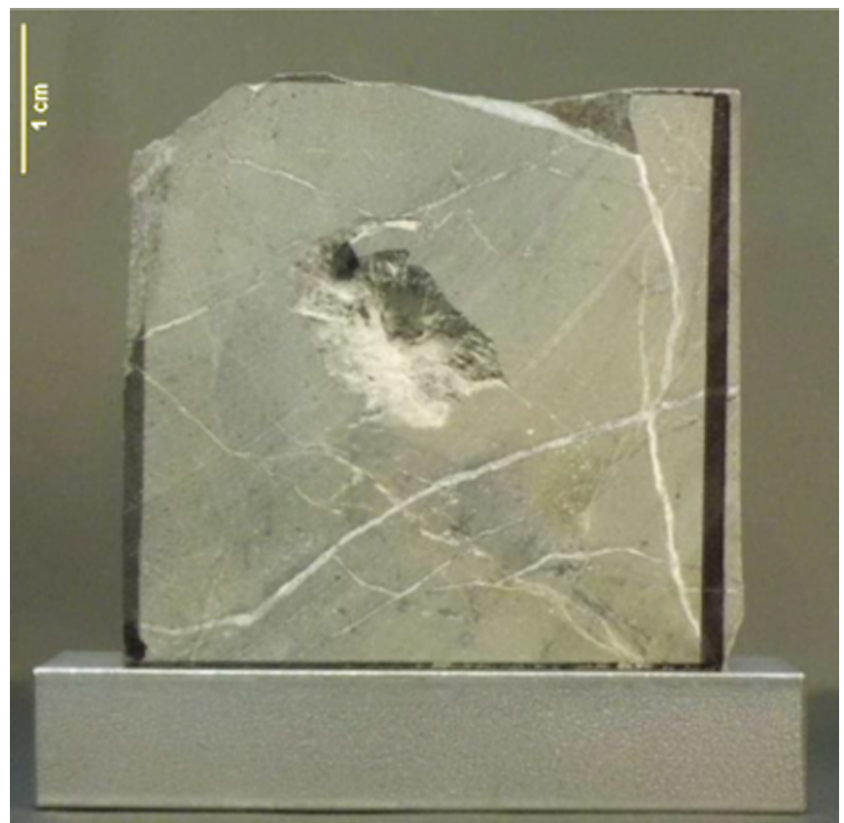
2.2 | Analogue shock experiments

To simulate the effects of impact on the planetary surface, the sample was targeted using a two-stage light gas gun located at the University of Kent, UK.[44] The sample was impacted with a high velocity stainless steel millimetre-sized projectile, fired at the sample at a speed of 5 km/s. Figure 2 shows the impact crater in the centre of the sample. The white calcite veinlets do not intersect with the cratered region. Following the impact, the ejecta from the crater were collected, for comparison with basalt at the immediate margin of the crater (assumed shocked) and distant from the crater (assumed unshocked).

2.3 | Raman spectroscopy analysis of analogue sample (shocked and unshocked)

The ExoMars RLS is a vibrational spectroscopy instrument that is designed to detect spectral bands across the 150- to 3800-cm^{-1} wavenumber offset range. Incorporating a green (532 nm) laser, an efficient grating-based spectrometer, a high performance scientific camera and a specifically designed optical head unit, the instrument will scan the surface of crushed drill extracts with a 50-μm laser spot and will generate spectra with a limiting band resolution of ∼6–8 cm^{-1}. Transect analyses will be performed by finely stepping the sample holder in specific directions during spectral acquisition campaigns.

In preparation for surface operations, an RLS instrument simulator has been developed which is located at the Centro de Astrobiologia in Spain.[39] The benchtop instrument was designed to replicate the key performance aspects of the RLS flight system and provide a method of performing and testing rover-like instrument operations.

The simulator system includes a two-dimensional sample distribution system that moves the sample in 2.5-μm steps beneath the instrument's optical head, emulating the ExoMars rover's Sample, Preparation, and Distribution System (SPDS)—see Figure 3a. The simulator also incorporates a Z-axis translation system with an integrated laser autofocusing system to ensure optimum spectroscopic signal. The optical head produces a 50-μm laser spot at the sample surface (the laser spot is visible on the surface of the sample in Figure 3b), and the system incorporates an internal context imager, which is used to provide close-up images of samples during spectral acquisitions (an example is shown in Figure 3c). The imaging system uses an identical optical path to the laser so that the position of the laser beam (and therefore the specific region of spectroscopic investigation) can be readily identified.

In this study, the simulator was used to perform detailed spectral analyses of the unshocked and shocked regions of the Helen's Bay analogue sample. The surface of the sample in the region of the impact crater was systematically mapped in order to accurately characterise material distribution and to determine variations in spectral signature arising from impact stresses.

Raman spectra were acquired from a number of different points along transects across the surface of the sample. In order to accurately replicate the SPDS system on ExoMars, the sample was moved in 100-μm steps (in the X direction for an initial transect and then in the Y direction for the following transects). In total, six individual transects of the sample surface were performed and ∼700 separate spectra were acquired from points along each transect line (see Figure 4a). Samples of ejecta material generated during the impact process were also analysed (i.e., spectra were acquired from random positions across the surface of the ejecta material, with each acquisition focusing on a single or small number of
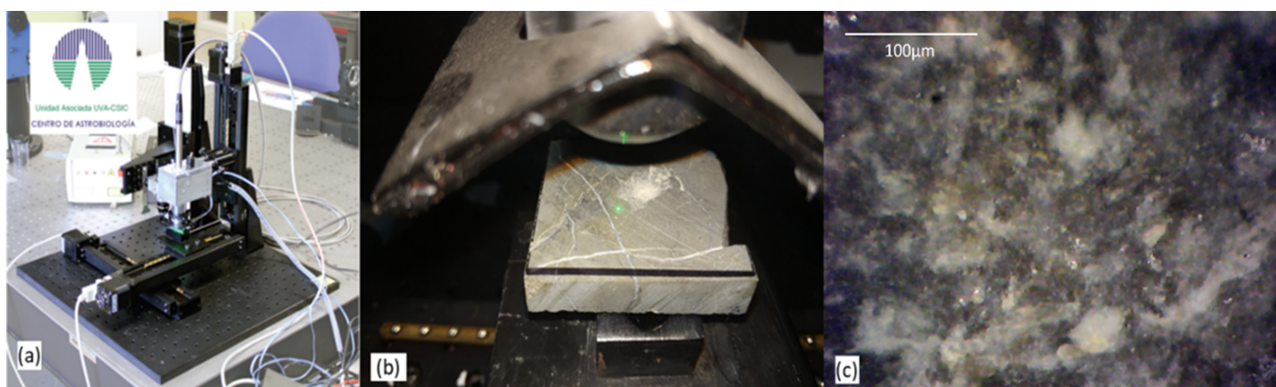

FIGURE 3 (a) The Raman laser spectrometer simulator, located in the Centro de Astrobiologia,[39] (b) the Helen's Bay sample positioned on the 2D sample distribution system, (c) context image acquired by the RLS simulator imager of a region containing a white vein on the sample surface

grains—see Figure 4b). At each and every sample point, the acquisition time and the number of stacked spectra were optimised (i.e., the signal-to-noise ratio of the strongest spectral bands was maximised), with acquisition times ranging from 2.5 to 19 s and the number of acquisitions ranging from 4 to 29. The laser irradiance at the sample was ~0.8 kW/cm^2, and fluorescence detection and removal processes[45] were applied to the spectra acquired at each spot.

3 | RESULTS

In order to fully investigate the effects that the impacts have on the spectra produced by the sample, the sample was divided into four separate components of interest: (i) the unshocked sample (i.e., material that serves as the sample background), (ii) the crater region, (iii) veinlets crossing the surface, and (iv) the ejecta collected following the shock experiments. The background and crater regions were defined by their relative depths with respect to the surface of the sample. The magnitude of the depth of each region was derived using the Z-position of the laser focus point on the sample surface (obtained by the autofocusing mechanism at each transect point). Figure 5 shows the depth profile generated from the first transect performed. Based on this profile, material sampled at depths above −300 μm was defined as the sample background material (i.e., unshocked material) whilst material sampled at depths below −300 μm was classified as being part of the cratered region (i.e., shocked material).

The regions containing veinlet material were identified using the images collected by the instrument's context imager. Images were acquired at each transect position: Figure 6 shows one example image that was acquired from the background region on the surface of the sample, including a millimetre-sized white vein.

Figure 7 shows a cross-sectional diagram of the sample, highlighting the different regions of interest and the forces involved in the impact. The figure also shows typical spectra from each region; the background, the crater and the ejecta. The spectrum (a) acquired form the
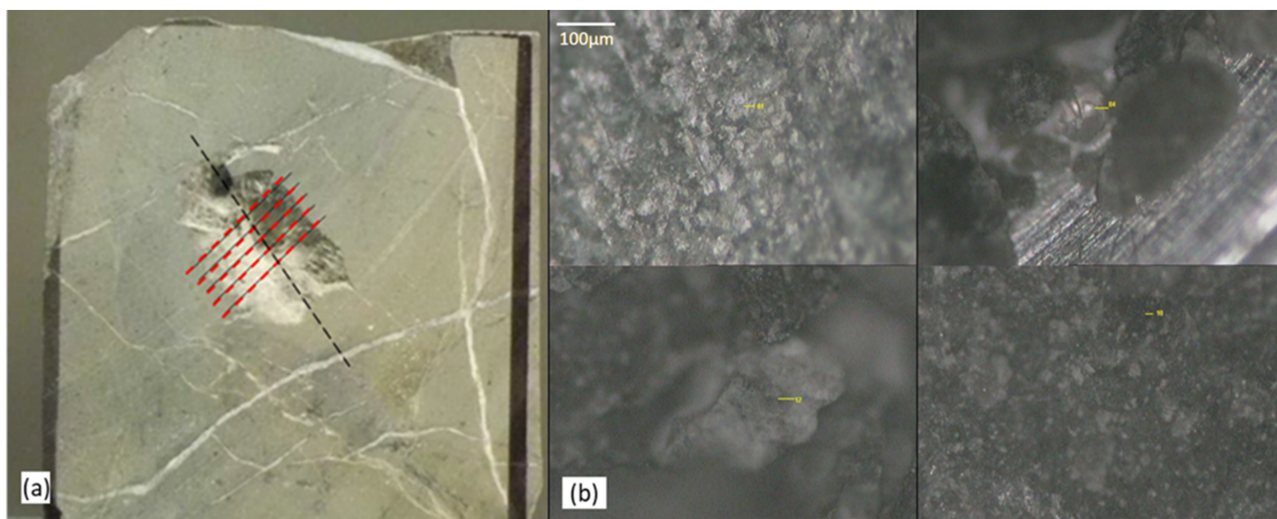

FIGURE 4 (a) The surface of the Helen's Bay basalt sample, highlighting the position of the initial transect (black) and the repeated transects (red). Panel (b) shows four examples of context images acquired from the ejecta material
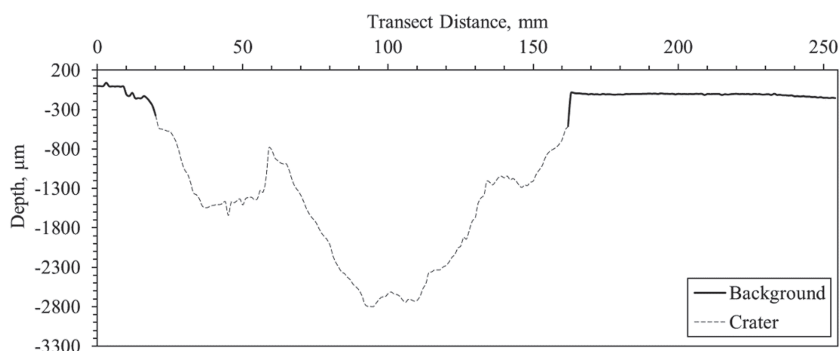
FIGURE 5 Depth profile of the shocked sample, measured using the optimum focal position of the instrument laser
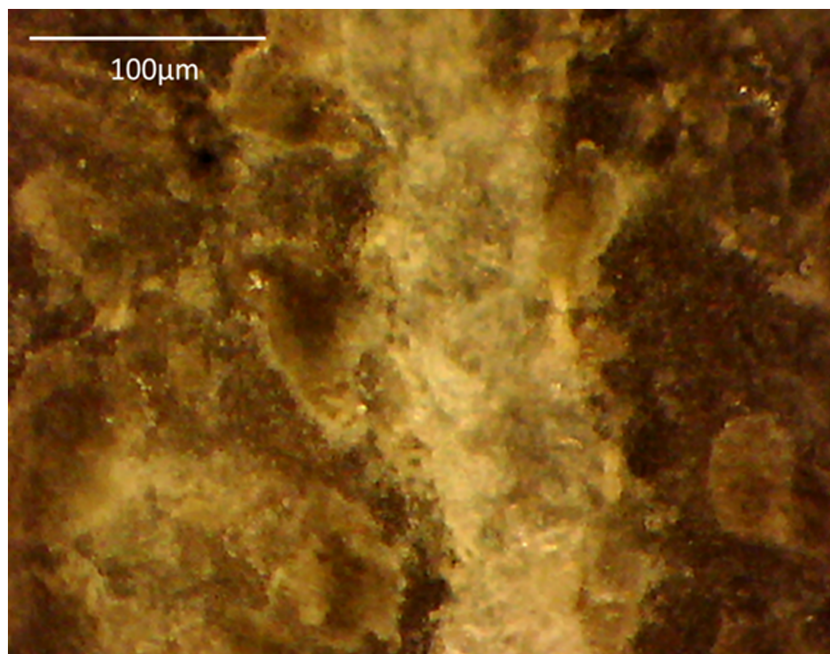
FIGURE 6 Context image acquired during the first transect across the Helen's Bay sample. The 350 × 350 μm image was acquired from the uncratered region of the sample and shows a white vein through the darker background rock
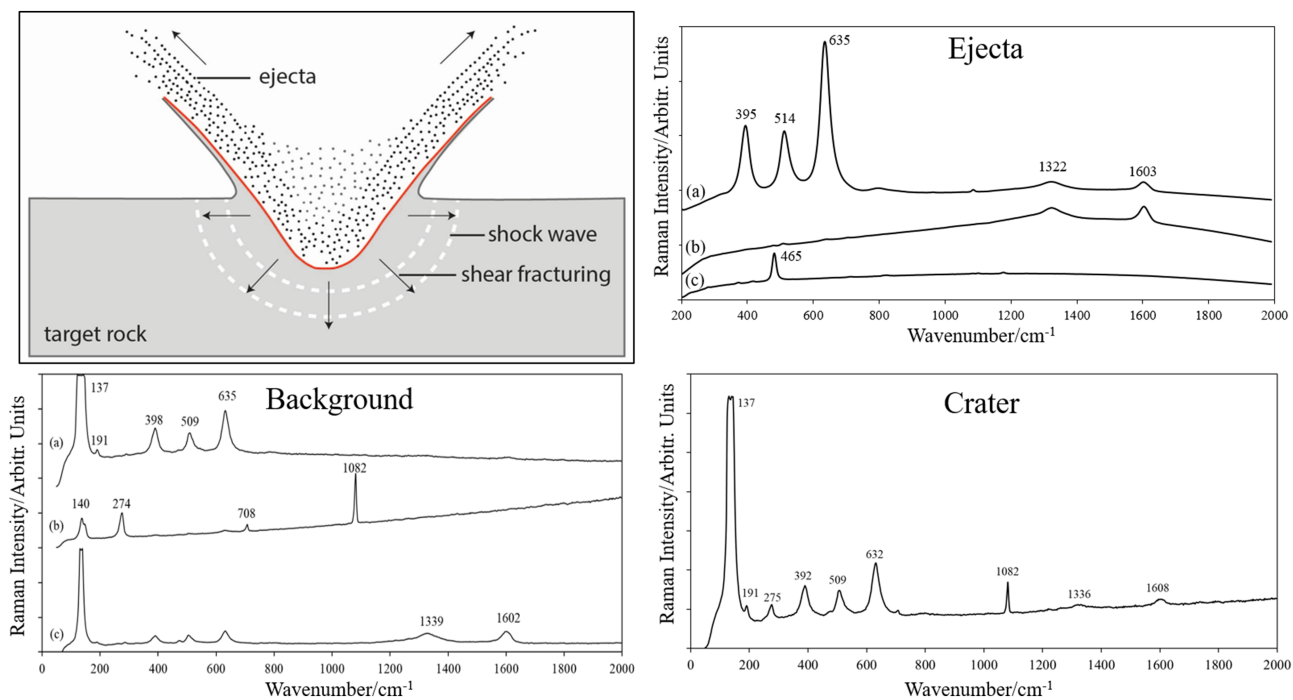
FIGURE 7 Schematic of the impact process, highlighting the different target regions (i.e., ejecta, crater, and background), surrounded by example spectra acquired from each target region. Section modified after Kenkmann et al.[46]

background contains strong anatase bands at 137, 398, 509, and 635 cm^{-1} and a weaker band at 190 cm^{-1}. Spectrum (b) shows clear calcite bands at 1082, 708, and 274 cm^{-1}, with the 150-cm^{-1} band appearing as a shoulder feature on the ~140-cm^{-1} anatase band. A weaker anatase signature can also be seen in spectrum (c), but

more significantly, the spectrum shows the presence of reduced carbon, indicated by the presence of the D and G bands at 1339 and 1602 cm^{-1}, respectively.

Like the spectra acquired from the background material, the crater spectra include evidence of calcite, with bands at 277, 708, and 1082 cm^{-1} all present. The crater

spectra also exhibit strong bands at 136, 190, 398, 509, and 634 cm^{-1} that are likely to be associated with the presence of anatase. Spectra obtained from the cratered region also exhibit carbon D and G bands (situated at 1339 and 1602 cm^{-1}, respectively), verifying the presence of reduced carbon in those regions too.
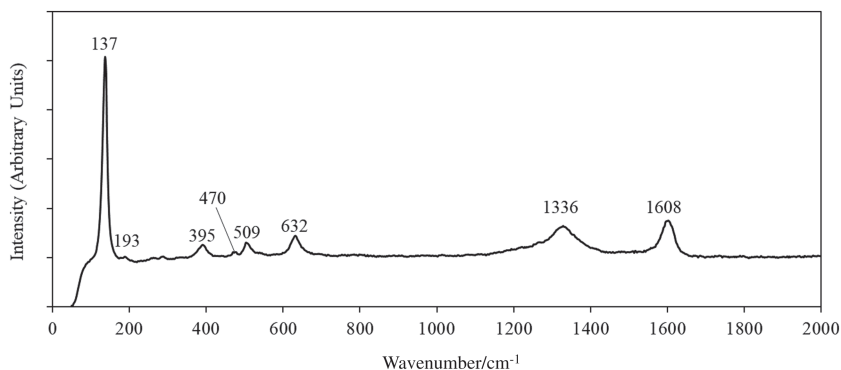
The spectra acquired from the ejecta material also show evidence for the presence of reduced carbon spectra (a) and (b) both contain the carbon D and G bands (with the presence of a strong anatase signatures in spectrum (a)). In contrast, spectrum (c) only shows Raman band at 465 cm^{-1}, which is usually associated with quartz. No other spectral bands features are present in the spectrum, including any evidence of reduced carbon.

One example of a spectrum acquired from the veinlet material is shown in Figure 8. Again, the presence of bands at 137, 190, 395, 510, and 632 cm^{-1} provides strong evidence for the presence of anatase, and the bands at 1333 and 1602 cm^{-1} indicate the presence of reduced carbon.

The spectra collected from all four parts of the analogue sample indicate that reduced carbon is present throughout the material. This is important because the characteristics of the D and G bands can be used to determine if the shock process has an impact on the amount of molecular order within the carbonaceous material. More specifically, by assessing the characteristics of the G bands present in the spectra obtained from each region of the sample (i.e., the position and full width half maximum [FWHM]), the relative level of thermal maturity can be determined. Consequently, the G band centroid position and the FWHM of the peak were obtained for each of the spectra collected. In each case, a non-linear background subtraction was performed in a small window ($\sim$100 cm^{-1}) around the band before a spectral fit was performed on the resulting G-band profile to accurately determine the band position and width. To ensure a robust set of parameters, this process was only performed on G-bands that exhibited a signal-to-noise ratio greater than 5.

Figure 9 shows a cross-plot of the carbon G-band positions and FWHM obtained using this procedure for spectra acquired from the three separate sample regions (i.e., the background, the cratered region, and the ejecta

FIGURE 8 Spectrum acquired from the veinlet material. The weak band at 470 cm^{-1} indicated the presence of quartz
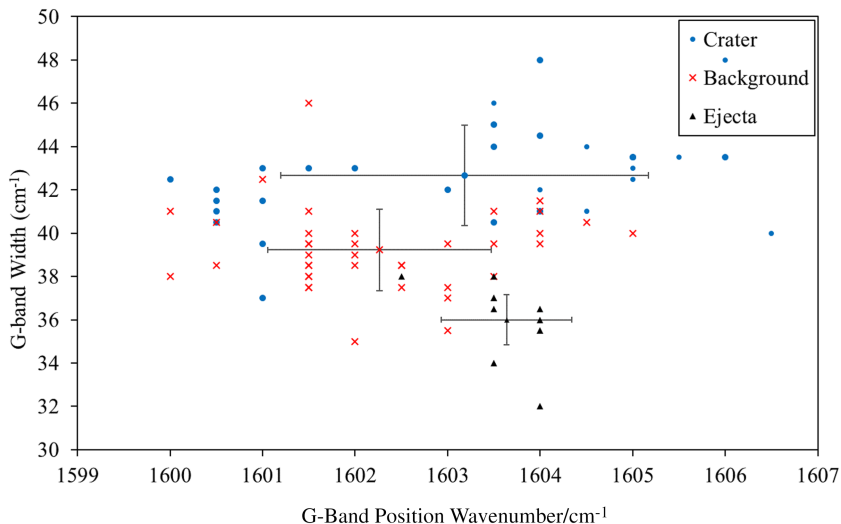
FIGURE 9 Cross-plot showing the characteristics of the carbon G-band featured in spectra acquired from the sample background, the crater material, and the shock ejecta. The points with the error bar indicate the average position of G bands from that region, with the errors bars representing the standard deviation of the data set

material). The plot clearly reveals the presence of three distinct carbon populations. The G bands observed in the crater material exhibit a shift to greater band width (an increase of ~3 cm^{-1}) compared to the material sampled in the background region, implying that the shocked material has a lower level of structural order and thermal maturity.[26] Furthermore, as a population, the G-bands acquired from the ejecta material exhibit a narrowing of band width (~3 cm^{-1}) in comparison to the background. This implies that the ejecta material has a greater level of thermal maturity.

Equivalent parameters for the carbon D band were also obtained using the same background and fitting processes described earlier, and the ratio between the D and G band intensities (I_D/I_G) were derived. This parameter has been demonstrated to show a strong correlation to the temperature of metamorphic processes in other studies.[26] Figure 10 shows the relationship between the carbon band intensity ratio, I_D/I_G, and metamorphism temperature (calculated by Beyssac et al.[47] and Kouketsu et al.[48]). The I_D/I_G derived from the background and crater spectra obtained from the Helen's Bay sample are included in the figure. The points have been plotted to align with the trend presented by the data from Kouketsu et al.[48] to derive a temperature for the two sample regions. The positions on the plot with respect to the data implies that the temperature associated with the reduced carbon in the background material is higher than that associated with the crater/shocked material.

4 | DISCUSSION

4.1 | Experimental conditions

The properties of the materials used in the experiment can be used to calculate the peak shock pressure achieved during impact. Using the Planar Impact Approximation,[49] we use a wave speed equation:

$$U_s = C + Su_\rho, \tag{1}$$

where C and S (defined by a linear relationship between shock wave and shock particle speeds U and u, respectively) and density (ρ) for both target and projectile materials are known. The values used are given in Table 1 and yield a peak shock pressure of 86 GPa. The shock pressure would have varied across the target. The ejecta will have two components. The fast ejecta (at high angle) from the central core of the crater will be highly shocked. However, ejecta that spalls off the surface in large platelets widen the crater and is at a lower shock pressure.

If the crater itself was sectioned and material examined from beneath the crater, the peak pressure falls off rapidly as shown in Parnell et al.[50]

4.2 | Raman data

The data obtained in this study verify that the RLS simulator is capable of detecting reduced carbon in basaltic

FIGURE 10 Relationship between the carbon band intensity ratio, I_D/I_G and the temperature at which the material underwent metamorphism (inferred by Beyssac et al.[47] and Kouketsu et al.[48]), overlain with the I_D/I_G derived from the background and crater material within the Helen's Bay sample

TABLE 1 Wave speed parameters for the basalt material in the sample and the stainless steel projectile

Material	C (m s^{-1})	S (no dimensions)	ρ (kg m^{-3})	Reference
Basalt	2600	1.62	3000	Density measured this study[50]
Stainless steel 304	4610	1.73	7800	Autodyn lookup tables[51]

material. The simulator was developed to closely imitate the performance characteristics of the RLS flight instrument; therefore, it is reasonable to assume that the RLS instrument on board the ExoMars rover will also be capable of detecting reduced carbon on the surface of Mars. This adds weight to studies performed by Hutchinson et al.[14] and Parnell et al.[38] on other flight-representative instrumentation. Reduced carbon is expected to be present on the surface of Mars as a result of meteorite bombardment, ancient volcanic activity, or microbial activity and, therefore, could be sampled by the ExoMars rover. The instrument's transect sampling scheme, along with the acquisition parameters used to acquire the spectra presented here are representative of those that will be employed by the RLS flight instrument during the mission. The fluorescence suppression algorithms used during this study have also been developed in preparation for the mission[45] and will play a key part in the detection of key mineral targets on Mars. Overall, it is clear that the operating mode deployed here is sufficient for the detection of reduced carbon in the sample.

Furthermore, the data also verify that the RLS simulator is capable of distinguishing between different populations of reduced carbon within a sample through the measurement of G-band characteristics. This is also consistent with previous studies[14,38] that demonstrated flight-like Raman spectrometers were able to discern between carbon populations of varying thermal maturity. Figure 7 shows that the spectra obtained from the background region of the sample exhibit average G-band positions and widths of ~1602 and 39 cm^{-1}, respectively. These measured characteristics are consistent with values previously reported by Parnell et al.[38] for Raman measurements of the reduced carbon found in the Helen's Bay sample.

The G-band positions and widths observed in the ejecta material are observed to be 1603.5 and 36 cm^{-1}, respectively. It should be noted that of the two parameters, the width of the carbon G-band is more sensitive to changes in thermal maturity.[51] Therefore this decrease in width of >3 cm^{-1} (compared with background material) implies that the ejecta material is of greater thermal maturity than the background material.

4.3 | Carbon ordering on shocked surface

The higher wavenumber position of the carbon G-band observed for the spectra obtained from the cratered region implies the material has a lower thermal maturity[26] compared with the background material (i.e., the crater material is more graphitic[52,53]). This implies that the projectile impact decreased the order of reduced carbon within the basalt sample. In contrast, previous studies have shown that burial and compression often increase the order and, therefore, the thermal maturity of carbonaceous material over time.[54,55] Further to this, Figure 10 shows that the I_D/I_G ratios of the spectra obtained from material within the cratered regions are systematically greater than that observed from spectra obtained from material in the background region of the analogue sample material. Compared with the metamorphic temperature data presented by Kouketsu et al.[48] and Beyssac et al.,[43] the difference in I_D/I_G ratio observed in this sample implies that the metamorphism temperature of the crater and background are 377 $\pm$ 20°C and 436 $\pm$ 14°C, respectively. Clearly, the temperatures cannot represent maximum thermal maturity, and the temperature must instead be regarded as a parameter that reflects thermal history.

The crater left by meteorite impact, or experimental projectile impact, has clearly experienced very high shock. It might be expected, therefore, that this would be expressed in the Raman characteristics of mineral phases in the rock. In the case of carbon, greater modification would be evident by increasing graphitisation. However, it is becoming apparent from terrestrial environments of very high stress that the irreversibility of graphitisation cannot be assumed. At the boundaries of tectonic plates, where fault slip causes earthquakes, measurements of carbon in the sheared rocks show that are actually less graphitic.[56–60] This so-called 'amorphisation of graphite'[58,60] is also evident in the shocked rock from the impact experiment.

Deformation in impact craters involves locally intense shearing and associated heating of the crater substrate, which is evident in hypervelocity experiments.[61–63] The sheared region may experience pressures of hundreds of megapascals.[63] Detailed modelling of the Chicxulub impact, a large crater implicated in large-scale biological extinction, concluded shear stresses over the range 0 to 19 MPa over a period of 300 s as the crater progressively evolved.[64] For comparison, a fault displaced during the 1999 Chi-Chi earthquake in Taiwan, which caused amorphisation of graphite,[57] experienced a shear stress of 0.95 to 1.30 MPa. Faults break at shear stresses from megapascals to tens of megapascals.[65,66]

The relatively low alteration evident in the ejecta is consistent with previous experimental observations. In the near-surface, spallation ejecta may be unshocked or weakly shocked.[67-70] This is important to the concept of panspermia in which microbial life could be transferred from one planetary surface to another by passage in meteorite ejecta.[67,69]

The decreased carbon ordering observed in the experimental crater generated by the impact confirms that shock forces within basaltic material may produce more reactive carbon. This has implications for potential (past) habitability on Mars because impacted, reduced carbon may become more biologically accessible,[50] providing regions of material that could be a microbial feedstock. The data presented here suggests that not only will the RLS flight instrument be able to detect regions of reduced carbon but that it will also be able to characterise the contribution of impact shock at the landing site region, thereby enhancing our assessment of habitability on the surface of Mars.

5 | CONCLUSION

The results obtained from the Raman analysis of a shocked Nakhla meteorite analogue using the ExoMars RLS simulator demonstrate that instrumentation similar in design and performance to the ExoMars flight instrument can detect reduced carbon within basaltic material. Furthermore, the data also show that such instrumentation, used in conjunction with representative spectral acquisition parameters and sampling schemes, is also capable of differentiating between carbon populations of different thermal maturity that arise from high velocity impacts.

Differentiating between potentially different sources of reduced carbon and determining the different geological processes the material has undergone are important aspect of the RLS science goals for the ExoMars mission. As such, this study has provided valuable information regarding optimum instrument operation, measurement strategies, and data processing algorithms, particularly with regard to the detailed analysis of shocked carbonaceous material.

Analysis of the shocked and unshocked material within the sample indicate that high velocity impacts can reduce the level of ordering, and can, therefore, reduce the apparent level of thermal maturity of the material. This reduction in order generates more biologically accessible carbon (i.e., more graphitic carbon, which is chemically more reactive), thereby improving the potential habitability of the planetary surface.

ORCID

Hannah N. Lerman https://orcid.org/0000-0002-4753-5913

REFERENCES

[1] J. J. Freeman, A. Wang, K. E. Kuebler, B. L. Jolliff, L. A. Haskin, *Can. Mineral.* **2008**, *46*, 6.

[2] S. E. J. Villar, H. G. Edwards, *Anal. Bioanal. Chem.* **2006**, *384*, 1.

[3] J. Jehlička, H. G. M. Edwards, P. Vítek, *Planet. Space Sci.* **2009**, *57*, 5.

[4] S. Maurice, R. C. Wiens, P. Bernardi, P. Caïs, S. Robinson, T. Nelson, O. Gasnault, J. M. Reess, M. Deleuze, F. Rull, J. A. Manrique, *Space Sci. Rev.* **2021**, *217*, 3.

[5] L. Beegle, B. Rohit, EGU General Assembly Conference Abstracts **2016**, 11215.

[6] F. Rull, S. Maurice, I. Hutchinson, A. Moral, C. Perez, C. Diaz, M. Colombo, T. Belenguer, G. Lopez-Reyes, A. Sansano, O. Forni, Y. Parot, N. Striebig, S. Woodward, C. Howe, N. Tarcea, P. Rodriguez, L. Seoane, A. Santiago, J. A. Rodriguez-Prieto, J. Medina, P. Gallego, R. Canchal, P. Santamaría, G. Ramos, J. L. Vago, *Astrobiology* **2017**, *17*, 627.

[7] J. Vago, O. Witasse, H. Svedhem, P. Baglioni, A. Haldemann, G. Gianfiglio, T. Blancquaert, D. McCoy, R. de Groot, *Sol. Syst. Res.* **2015**, *49*, 518.

[8] H. Svedhem, J. L. Vago, AGU Fall Meeting Abstracts, **2016**; P24C-09.

[9] J. L. Vago, F. Westall, A. J. Coates, R. Jaumann, O. Korablev, V. Ciarletti, I. Mitrofanov, J. L. Josset, M. C. De Sanctis, J. P. Bibring, F. Rull, *Astrobiology* **2017**, *17*, 6.

[10] C. Quantin-Nataf, J. Carter, L. Mandon, P. Thollot, M. Balme, M. Volat, L. Pan, D. Loizeau, C. Millot, S. Breton, E. Dehouck, *Astrobiology* **2021**, *21*, 3.

[11] C. Quantin-Nataf, J. Carter, L. Mandon, M. Balme, P. Fawdon, J. Davis, P. Thollot, E. Dehouck, L. Pan, M. Volat, C. Millot, Ninth International Conference on Mars **2019**, 2089.

[12] G. Ramos, M. Sanz-Palomino, A. G. Moral, C. P. Canora, T. Belenguer, R. Canchal, J. A. R. Prieto, A. Santiago, C. Gordillo, D. Escribano, G. Lopez-Reyes, *Proc. Soc. Photo-Opt. Instrum. Eng.* **2017**, 10377, 103770O.

[13] I. H. Rodriguez, G. Lopez-Reyes, D. R. Llanos, F. R. Perez, *Mathematics of Planet Earth*, Springer, Berlin, Heidelberg **2014** 127.

[14] I. B. Hutchinson, J. Parnell, H. G. Edwards, J. Jehlicka, C. P. Marshall, L. V. Harris, R. Ingley, *Planet. Space Sci* **2014**, *103*, 184.

[15] A. Steele, F. M. McCubbin, M. Fries, L. Kater, N. Z. Boctor, M. L. Fogel, P. G. Conrad, M. Glamoclija, M. Spencer, A. L. Morrow, M. R. Hammond, *Science* **2012**, *337*, 6091.

[16] M. Y. Zolotov, E. L. Shock, *Meteorit. Planet. Sci.* **2000**, *35*, 629.

[17] L. Becker, B. Popp, T. Rust, J. L. Bada, *Earth Planet. Sci. Lett.* **1999**, *167*, 71.

[18] D. S. McKay, E. K. Gibson, K. L. Thomas-Keprta, H. Vali, C. S. Romanek, S. J. Clemett, X. D. Chillier, C. R. Maechling, R. N. Zare, *Science* **1996**, *273*, 924.

[19] I. P. Wright, M. M. Grady, C. T. Pillinger, *Geochim. Cosmochim. Acta* **1992**, *56*, 2.

[20] E. K. Gibson Jr., D. S. McKay, S. J. Clemett, K. L. Thomas-Keprta, S. J. Wentworth, F. Robert, A. B. Verchovsky, I. P.

Wright, C. T. Pillinger, T. Rice, B. Van Leer, *Proc. Soc. Photo-Opt. Instrum. Eng.* **2006**, *6309*, 630901.

[21] H. Y. McSween Jr., *Rev. Geophys.* **1985**, *23*, 4.

[22] B. Sutter, A. C. Mcadam, P. R. Mahaffy, D. W. Ming, K. S. Edgett, E. B. Rampe, J. L. Eigenbrode, H. B. Franz, C. Freissinet, J. P. Grotzinger, A. Steele, *J. Geophys. Res.: Planets* **2017**, *122*, 12.

[23] Y. Wang, D. C. Alsmeyer, R. L. McCreery, *Chem. Mater.* **1990**, *2*, 5.

[24] F. Tuinstra, J. L. Koenig, *J. Chem. Phys.* **1970**, *53*, 1126.

[25] B. Sauerer, P. R. Craddock, M. D. Aljohani, K. L. Alsamadony, W. Abdallah, *Int. J. Coal Geol.* **2017**, *173*, 150.

[26] D. G. Henry, I. Jarvis, G. Gillmore, M. Stephenson, *Earth-Sci. Rev.* **2019**, *198*, 102936.

[27] D. M. Bower, A. Steele, M. D. Fries, L. Kater, *Astrobiology* **2013**, *13*, 103.

[28] J. Jehlička, P. Urban, J. Pokorný, *Spectrochim. Acta, Part a* **2003**, *59*, 2341.

[29] C. P. Marshall, H. G. M. Edwards, J. Jehlička, *Astrobiology* **2010**, *10*, 229.

[30] J. S. Lupoi, L. P. Fritz, T. M. Parris, P. C. Hackley, L. Solotky, C. F. Eble, S. Schlaegle, *Front. Energy Res.* **2017**, *5*, 24.

[31] J. S. Schmidt, R. Hinrichs, C. V. Araujo, *Int. J. Coal Geol.* **2017**, *173*, 1.

[32] A. C. Ferrari, J. C. Meyer, V. Scardaci, C. Casiraghi, M. Lazzeri, F. Mauri, S. Piscanec, D. Jiang, K. S. Novoselov, S. Roth, A. K. Geim, *Phys. Rev. Lett.* **2006**, *97*, 187401.

[33] H. G. Changela, J. C. Bridges, *Meteorit. Planet. Sci.* **2010**, *45*, 1847.

[34] L. J. Hicks, J. C. Bridges, S. J. Gurman, *Geochim. Cosmochim. Acta* **2014**, *136*, 194.

[35] J. C. Bridges, S. P. Schwenzer, *Earth Planet. Sci. Lett.* **2012**, *359*, 117.

[36] J. Farquhar, K. Sang-Tae, A. Masterson, *Earth Planet. Sci. Lett.* **2007**, *264*, 1.

[37] J. Fritz, A. Greshake, D. Stöffler, *Antarct. Meteorite Res.* **2005**, *18*, 96.

[38] J. Parnell, S. McMahon, N. J. F. Blamey, I. B. Hutchinson, L. V. Harris, R. Ingley, H. G. M. Edwards, E. Lynch, M. Feely, *Int. J. Astrobiol.* **2014**, *13*, 2.

[39] G. Lopez-Reyes, F. Rull, G. Venegas, F. Westall, F. Foucher, N. Bost, A. Sanz, A. Catalá-Espí, A. Vegas, I. Hermosilla, A. Sansano, J. Medina, *Eur. J. Mineral.* **2013**, *25*, 721.

[40] E. N. Sharpe, *Ir. Nat. J.* **1970**, *16*, 299.

[41] L. E. Craig, *Trans. R. Soc. Edinburgh: Earth Sci.* **1984**, *74*, 183.

[42] M. R. Lee, T. Tomkinson, D. F. Mark, F. M. Stuart, C. L. Smith, *Meteorit. Planet. Sci.* **2013**, *48*, 224.

[43] A. Steele, F. M. McCubbin, M. D. Fries, *Meteorit. Planet. Sci.* **2016**, *51*, 2203.

[44] M. J. Burchell, M. J. Cole, J. A. M. McDonnell, J. C. Zarnecki, *Meas. Sci. Technol.* **1999**, *10*, 41.

[45] G. Lopez-Reyes, F. Rull, *J. Raman Spectrosc.* **2017**, *48*, 1654.

[46] T. Kenkmann, M. G. Poelchau, G. Wulf, *J. Struct. Geol.* **2014**, *62*, 156.

[47] O. Beyssac, B. Gofféa, J.-P. Petitet, E. Froigneux, M. Moreau, J.-N. Rouzaud, *Spectrochim. Acta, Part a* **2003**, *59*, 2267.

[48] Y. Kouketsu, T. Mizukami, H. Mori, S. Endo, M. Aoya, H. Hara, D. Nakamura, S. Wallis, *Isl. Arc* **2014**, *23*, 33.

[49] H. J. Melosh, *Impact Cratering: A Geologic Process*, Clarendon Press, Oxford **1989**.

[50] J. Parnell, S. Bowden, P. Lindgren, M. J. Burchell, D. Milner, E. C. Baldwin, I. A. Crawford, *Meteorit. Planet. Sci.* **2010**, *45*, 1340.

[51] D. K. Muirhead, J. Parnell, S. Spinks, S. A. Bowden, Geological Society, London, Special Publications **2017**, *448*, 71.

[52] A. Schito, S. Corrado, Geological Society, London, Special Publications **2020**, *484*, 107.

[53] Q. Zhou, X. Xiao, L. Pan, H. Tian, *Int. J. Coal Geol.* **2014**, *121*, 19.

[54] P. R. Buseck, O. Beyssac, *Elements* **2014**, *10*, 421.

[55] S. R. Kelemen, H. L. Fang, *Energy Fuels* **2001**, *15*, 653.

[56] M. Kirilova, V. Toy, J. S. Rooney, C. Giorgetti, K. C. Gordon, C. Collettini, T. Takeshita, *Solid Earth* **2018**, *9*, 223.

[57] T. Hirono, Y. Maekawa, H. Yabuta, *Geochem., Geophys., Geosyst.* **2015**, *16*, 1233.

[58] Y. Nakamura, K. Oohashi, T. Toyoshima, M. Satish-Kumar, J. Akai, *J. Struct. Geol.* **2015**, *72*, 142.

[59] H. Mukoyoshi, D. Kaneki, T. Hirono, *Earth Planets Space* **2018**, *70*, 1.

[60] S. Kaneki, T. Hirono, *Sci. Rep.* **2019**, *9*, 1.

[61] C. A. Polanskey, T. J. Ahrens, *Icarus* **1990**, *87*, 140.

[62] P. H. Schultz, *J. Geophys. Res.* **1996**, *101*, 21117.

[63] R. Winkler, R. Luther, M. H. Poelchau, K. Wünnemann, T. Kenkmann, *Meteorit. Planet. Sci.* **2018**, *53*, 1733.

[64] A. S. P. Rae, G. S. Collins, M. Poelchau, U. Riller, P. M. Davison, R. A. F. Grieve, G. R. Osinski, J. V. Morgan, IODP-ICDP Expedition 364 Scientists, *J. Geophys. Res.: Planets* **2019**, *124*, 396.

[65] H. Sone, T. Uchide, *Tectonophysics* **2016**, *684*, 63.

[66] A. Copley, *J. Geol. Soc.* **2018**, *175*, 1.

[67] P. Fajardo-Cavazos, F. Langenhorst, H. J. Melosh, W. N. Nicholson, *Astrobiology* **2009**, *9*, 647.

[68] K. J. P. Lakshmi, P. S. Kumar, *J. Geophys. Res.: Planets* **2020**, *125*, e2020JE006593.

[69] M. K. Wallis, N. C. Wickramasinghe, *Earth Planet. Sci. Lett.* **1995**, *130*, 69.

[70] T. Kenkmann, F. Schönian, *Meteorit. Planet. Sci.* **2006**, *41*, 1587.